

Multi-angle holographic characterization of individual fractal aggregates

Rafe Abdulali,¹ Lauren E. Altman,² and David G. Grier²

¹*Packer Collegiate Institute, Brooklyn, NY 11201, USA*

²*Department of Physics and Center for Soft Matter Research,
New York University, New York, NY 10003, USA*

Holographic particle characterization uses quantitative analysis of holographic microscopy data to precisely and rapidly measure the diameter and refractive index of individual colloidal spheres in their native media. When this technique is applied to inhomogeneous or aspherical particles, the measured diameter and refractive index represent properties of an effective sphere enclosing each particle. Effective-sphere analysis has been applied successfully to populations of fractal aggregates, yielding an overall fractal dimension for the population as a whole. Here, we demonstrate that holographic characterization also can measure the fractal dimensions of an individual fractal cluster by probing how its effective diameter and refractive index change as it undergoes rotational diffusion. This procedure probes the structure of a cluster from multiple angles and thus constitutes a form of tomography. Here we demonstrate and validate this effective-sphere interpretation of aspherical particles' holograms through experimental studies on aggregates of silica nanoparticles grown under a range of conditions.

I. INTRODUCTION

Many colloidal particles of natural and industrial interest are formed by random aggregation of nanometer-scale monomeric units. Examples include protein aggregates in biopharmaceutical products [1], haze in beer, soot from flames, astronomical dust particles, nanoparticle agglomerates in precision polishing slurries [2] and microplastics in the environment [3]. Standard optical methods for particle characterization, such as static and dynamic light scattering, yield population-averaged views of such particles' structural properties [4, 5]. Particle-resolved characterization measurements based on holographic microscopy in principle could probe the structure of individual fractal aggregates [6], but so far have been used to study the average properties of populations of aggregates [7–9]. Here, we demonstrate a fast and effective method to assess the structural properties of individual colloidal fractal aggregates from sequences of holograms recorded at multiple angles.

Each hologram of a fractal aggregate encodes information about the particle's three-dimensional structure [6–8]. Extracting that information with light-scattering theory is a high-dimensional inverse problem [10] whose numerical convergence is both slow and uncertain. The corresponding analysis for a homogeneous sphere, by contrast, converges rapidly and yields precise values for the sphere's diameter and refractive index [11]. Applying the efficient spherical-particle analysis to a hologram of a fractal cluster yields values for the diameter and refractive index that characterize an effective sphere [7, 9] comprised of the cluster itself and the fluid that fills its pores. This approach builds on the recent observation that effective-sphere analysis can be used to measure the orientation of colloidal dimers in shear flows [12]. For an irregularly shaped cluster, these effective-sphere values depend on both the cluster's orientation and also its morphology [6, 7]. Previous experimental studies recorded a single hologram of each cluster in a population and com-

bined effective-sphere results to infer information about the particles' morphology [7, 8]. This approach presumes that all of the clusters in the population are grown under similar conditions so that their results can be combined meaningfully.

Here, we record holographic videos of individual fractal clusters as they undergo translational and rotational diffusion. This protocol yields holograms of each cluster in multiple orientations. When analyzed with the effective-sphere analysis, the set of measurements provides insights into the morphology of that specific cluster. Single particle morphological analyses then can be compared with holographic analysis of the population as a whole performed with single snapshots of clusters in a flowing fluid.

II. HOLOGRAPHIC PARTICLE CHARACTERIZATION IN THE EFFECTIVE-SPHERE APPROXIMATION

In-line holographic microscopy uses a collimated laser beam to illuminate the sample [13]. Light scattered by colloidal particles in the sample interferes with the rest of the illumination. An optical microscope magnifies the interference pattern and relays it to a video camera, which records its intensity. Each image in the video stream is a hologram of the particles in the observation volume that encodes information about the particles' positions and compositions. That information can be extracted by fitting a recorded hologram to a generative model for the image formation process.

We model the illumination as a monochromatic plane wave that is linearly polarized along \hat{x} and propagates along \hat{z} :

$$\mathbf{E}_0(\mathbf{r}) = u_0 e^{ikz} \hat{x}. \quad (1)$$

A small spherical particle located at \mathbf{r}_p scatters a wave,

$$\mathbf{E}_s(\mathbf{r}) = E_0(\mathbf{r}_p) \mathbf{f}_s(k(\mathbf{r} - \mathbf{r}_p)), \quad (2)$$

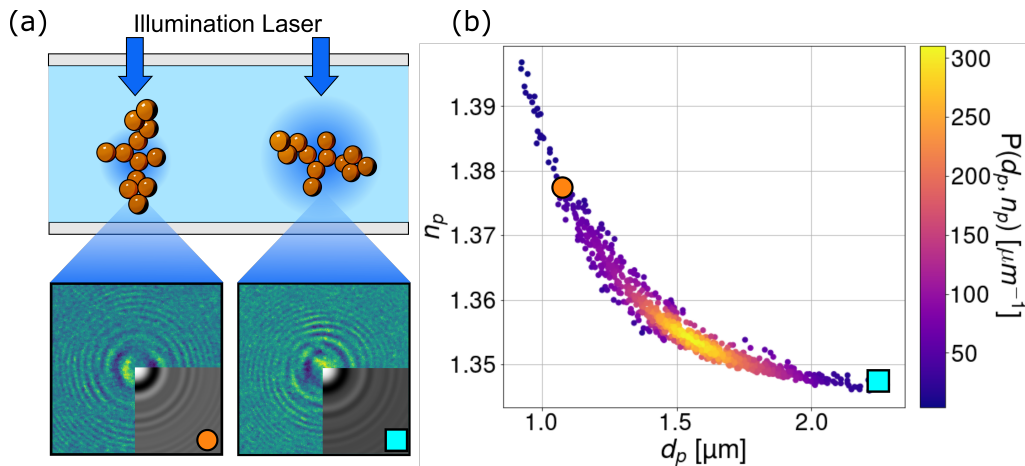


FIG. 1. (a) Schematic representation of holographic characterization of a diffusing fractal aggregate in a microfluidic channel. The aggregate, passing through the illuminating laser beam, scatters light that interferes with the rest of the laser beam to create a hologram. The two images are experimental holograms of a single aggregate in different orientations with fits to Lorenz-Mie theory superimposed in the lower-right quadrants. (b) Effective values for d_p and n_p for the aggregate in multiple orientations. Each plot symbol corresponds to a single observation of the freely diffusing cluster and is colored by the density of observations, $P(d_p, n_p)$. Orange and teal symbols denote results from the holograms in (a).

that is proportional to the incident field at its position. The structure of the scattered wave is described by the Lorenz-Mie scattering function, $\mathbf{f}_s(k\mathbf{r})$ [14–16], which is parameterized by the sphere’s diameter, d_p , and its refractive index, n_p . The superposition of the incident and scattered waves creates an interference pattern whose intensity is recorded by the camera [11]:

$$b(\mathbf{r}) = \left| \hat{x} + e^{-ikz_p} \mathbf{f}_s(k(\mathbf{r} - \mathbf{r}_p)) \right|^2, \quad (3)$$

where we have normalized the recorded image [11] so that $u_0^2 = 1$. Distances are measured relative to the vacuum wavelength of light, λ , through the wave number, $k = 2\pi n_m/\lambda$, in a medium of refractive index n_m . In typical implementations, λ , n_m , and the magnification of the microscope are treated as fixed instrumental parameters. This generative model for the image-formation process can be fit to a measured hologram by optimizing \mathbf{r}_p , d_p and n_p . When applied to homogeneous colloidal spheres, this procedure finds the center of particle with a measurement error of $\sigma_x = \sigma_y = 2$ nm and $\sigma_z = 5$ nm. The same measurement yields the sphere’s diameter with a precision of $\sigma_d = 2$ nm and its refractive index with a precision of $\sigma_n = 0.001$ [17].

Equation (3) can be generalized to accommodate aspherical and inhomogeneous particles by selecting a suitable form for the scattering function [18]. Such generalizations, however, dramatically increase the time and resources needed to seek optimal solutions to the inverse problem [19]. The effective-sphere approximation avoids this computational cost by analyzing holograms of aspherical particles using the Lorenz-Mie scattering function for homogeneous spheres. In this case, optimal values for the diameter and refractive index reflect the properties of an effective sphere encompassing the particle

whose index may be interpreted with Maxwell Garnett effective-medium theory [20] to obtain information about the particle’s true underlying properties [7, 9, 21, 22]. A porous sphere, for example, consists of a base material of refractive index n_0 that comprises a fraction, ϕ , of its volume. The rest of the volume is filled with the fluid medium at refractive index n_m . The effective refractive index for such a two-component system is [9, 21]

$$n_p = \sqrt{\frac{1 + 2\phi L(n_0/n_m)}{1 - \phi L(n_0/n_m)}}, \quad (4a)$$

where the Lorentz-Lorenz function is

$$L(m) = \frac{m^2 - 1}{m^2 + 2}. \quad (4b)$$

Effective-sphere analysis can be applied to aggregates of nanoparticles, which tend to be aspherical as well as porous, provided that the aggregates’ asperities are small enough for effective-medium theory to apply [6–8]. The number, $N = (d_p/d_0)^D$, of monomers of diameter d_0 in a cluster of diameter d_p depends on the aggregation mechanism and is characterized by the fractal dimension, D . The monomers in such a cluster occupy a fraction

$$\phi(d_p) = \frac{Nd_0^3}{d_p^3} = \left(\frac{d_p}{d_0}\right)^{D-3} \quad (5)$$

of the aggregate’s volume, the rest being filled with the medium. This suggests that the effective refractive index of a fractal aggregate should scale with its diameter as [7]

$$\ln\left(\frac{L(m_p)}{L(m_0)}\right) = (D - 3) \ln\left(\frac{d_p}{d_0}\right), \quad (6)$$

where $m_p = n_p/n_m$ and $m_0 = n_0/n_m$. Equation (6) has been used successfully to assess the fractal dimension of populations of protein aggregates [8], and nanoparticle clusters [7], and has been validated through simulations of light scattering by fractals [6]. These numerical studies also suggest that Eq. (6) should hold for individual fractal clusters.

III. MULTI-ANGLE HOLOGRAPHY OF FRACTAL CLUSTERS

As illustrated in Fig. 1(a), a fractal aggregate's hologram changes as the the aggregate rotates, leading effective-sphere analysis to settle on different values for the effective diameter and refractive index. The data in Fig. 1(b) were obtained for a single fractal silica aggregate with each point representing one measurement of the freely-diffusing cluster. The two representative holograms in Fig. 1(a) are called out with large plot symbols in Fig. 1(b) and generally span the range of effective properties exhibited by this aggregate in different orientations. Such a distribution of values can be interpreted with Eq. (6) to obtain a tomographic estimate for the cluster's fractal dimension, D .

The tomographic value of D for an individual aggregate can be compared with the average scaling behavior obtained from single-hologram analysis of multiple clusters. This comparison constitutes a test of the assumption underlying previous holographic characterization studies [7, 8] that all of the fractal aggregates in a population scale in a similar way and that their scaling behavior can be captured by effective-sphere analysis. This test can be made more rigorous by performing measurements over a range of growth conditions designed to yield aggregates with different fractal dimensions.

Our model system consists of dispersions of silica nanospheres (Ludox TMA colloidal silica, Aldrich catalog no. 420859) that are induced to aggregate through the addition of salt. The spheres in this system have mean diameter $d_0 = 20$ nm as determined by dynamic light scattering (LS Spectrometer, LS Instruments; Zetasizer Nano ZS, Malvern Instruments). The stock dispersion has 34 wt% solids, which corresponds to a number density of $c = 5 \times 10^{16}$ mL⁻¹ assuming the density of silica to be $\rho_{\text{SiO}_2} = 2.2$ g cm⁻³. This stock solution is diluted with deionized water (MilliQ Ultrapure Water System, MilliporeSigma) and is destabilized by adding 0.1 M MgCl₂ (Sigma-Aldrich, CAS no. 7791-18-6). Aggregation is allowed to proceed for 1 h before the dispersion is further diluted with deionized water to arrest growth. Clusters from the diluted dispersion are then sampled immediately for analysis.

Holographic characterization of populations of aggregates is performed with a commercial instrument (xSight, Spheryx, Inc.) that automatically records and analyzes holograms of thousands of particles by drawing up to 6 μ L of sample through a microfluidic observation vol-

ume in a pressure-driven flow. Each detected particle is characterized by a single value for the diameter and refractive index. The microfluidic channel used for these measurements (xCell, Spheryx, Inc.) has a 50 μ m minimum dimension, which means that the concentration of micrometer-scale particles can be measured accurately at concentrations up to 10⁷ mL⁻¹ before neighboring particles' holograms overlap significantly.

Individual particles from each sample also were analyzed in a custom-built holographic microscope operating at a vacuum wavelength of $\lambda = 0.447$ μ m (Coherent Cube) and an effective system magnification of 48 nm/pixel. Samples were contained in microfluidic chambers formed by sealing the edges of a #1.5 glass cover slip to the surface of a standard glass microscope slide with UV-cured optical adhesive (NOA81, Norland Products). The 30 μ m nominal thickness of these chambers is large enough for an aggregate to diffuse freely in three dimensions. The holographic microscope therefore observes the aggregate in all orientations over time. The particle's tendency to diffuse out of the field of view was controlled using a holographic optical trapping system integrated into the instrument [23]. This instrument's camera (Flea3 monochrome USB3.1, Teledyne FLIR) records holograms at 30 frame/s with an exposure time of 10 μ s, which is fast enough to avoid motion blurring [24, 25] given the translational and rotational diffusion coefficients for a micrometer-diameter object,

$$D_r = \frac{k_B T}{3\pi\eta d_p} \approx 0.4 \mu\text{m}^2 \text{s}^{-1} \quad \text{and} \quad D_\theta = \frac{k_B T}{\pi\eta d_p^3} \approx 1.3 \text{s}^{-1}, \quad (7)$$

respectively, in a medium with viscosity $\eta = 1$ mPa.s. Single-particle holograms were analyzed with the open-source `pylorenzmi` package.

Aggregation at vanishingly low monomer concentration allows clusters to grow through diffusion-limited aggregation (DLA) [26] and yields clusters with fractal dimensions as large as $D = 2.3$. Destabilizing a more concentrated dispersion allows for diffusion-limited cluster aggregation (DLCA), which leads to more open and spindly structures with fractal dimensions around $D = 1.3$ [27].

The holographic characterization data in Fig. 2(a) and (b) were obtained for populations of 5000 silica aggregates grown at starting monomer concentrations of $c = 1.4 \times 10^{15}$ mL⁻¹ and 5.6×10^{15} mL⁻¹, respectively. Each point represents the measured diameter and refractive index of a single particle, recast into the form of Eq. (6) and is colored by the relative density of measurements, $\rho(d_p, n_p)$. Both sets of results generally follow the linear trend predicted by Eq. (6). Aggregates grown at lower monomer concentration have an inferred fractal dimension of $D = 1.39 \pm 0.33$ while those grown at higher concentration have a slightly lower value, $D = 1.27 \pm 0.34$, which is consistent with expectations for three-dimensional DLCA [27]. These ranges are overlaid as dashed lines in Fig. 2(a) and Fig. 2(b).

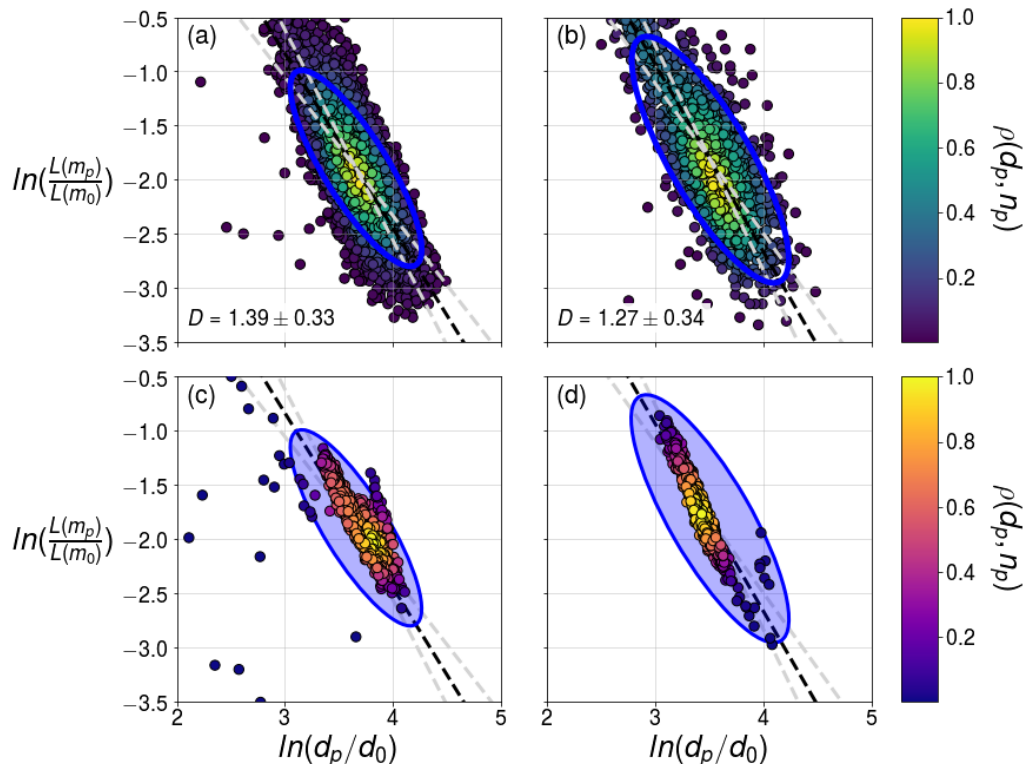


FIG. 2. Characterization data for two populations of particles formed by aggregating silica nanoparticles from an initial concentration of (a) 1.4×10^{15} nanoparticles/mL and (b) 5.6×10^{15} nanoparticles/mL. Each point represents the diameter, d_p , and refractive index, n_p , of a single aggregate, rescaled according to Eq. (6). Points are colored by the relative density of measurements, $\rho(d_p, n_p)$. Best-fit (dashed) lines show estimates for the population-averaged fractal dimension together with uncertainty bounds. (c) and (d) show multi-angle characterization results for individual aggregates sampled from the dispersions in (a) and (b), respectively. The $2\text{-}\sigma$ confidence ellipses and best-fit lines from (a) and (b) are reproduced to aid comparison between population-averaged and single-cluster results.

Multi-angle characterization of individual aggregates yields results that are consistent with population-averaged measurements. The data in Fig. 2(c) and (d) were obtained for aggregates drawn from the same populations as (a) and (b), respectively. Points in these scatter plots represent effective diameters and refractive indexes that are measured over time as the aggregate undergoes rotational diffusion. The associated population distributions are reproduced as $2\text{-}\sigma$ confidence ellipses to facilitate comparison. In both cases, the fractal dimension of the single-particle distribution agrees with that of the corresponding population.

Figure 3 shows how the population-averaged fractal dimension varies with monomer concentration over two decades from $c = 10^{14} \text{ mL}^{-1}$ to 10^{16} mL^{-1} . As expected, the clusters' fractal dimension is anticorrelated with the initial monomer concentration. The measured concentration of aggregates is 10^6 aggregates/mL in the most dilute samples, with a typical aggregate containing an estimated 5000 monomers. This suggests that no more than 5×10^9 monomers/mL have aggregated into clusters that are large enough to be detected. Most of the nanospheres therefore either remain in monomeric form or have formed aggregates smaller than the measurement

technique's detection limit of $d_p \lesssim 500 \text{ nm}$. Based on these estimates, the initial concentration of monomers is high enough to support cluster-cluster aggregation over the full range of growth conditions considered in this study and helps to further validate the observed range of fractal dimensions. While the population-averaged data show high variance, limiting the conclusions that can be confidently drawn, the data from the individual aggregate analysis are in agreement with our anticorrelation hypothesis.

IV. TRACKING ROTATIONAL DIFFUSION OF A FRACTAL AGGREGATE

Values of the diameter and refractive index inferred from effective-sphere analysis of an aspherical particle can be used to estimate the particle's instantaneous polar orientation angle, $\theta(t)$ [12]. As an illustrative example, we consider the single-particle data set from Fig. 2(c). The largest effective diameter and smallest effective refractive index is obtained when the particle's semi-major axis lies along the imaging plane, $\theta = 0$. The opposite end of the distribution is obtained when the semi-major

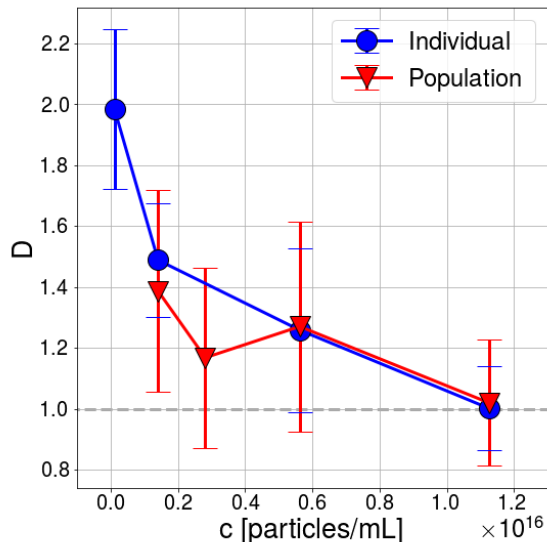


FIG. 3. Measured population-average fractal dimension as a function of initial nanoparticle concentration. Trend lines for both individual aggregates (blue circles) and populations of aggregates (red triangles) suggest an inverse relationship between concentration of nanoparticles c and fractal dimension D . The dashed line at $D = 1$ represents the lower physical limit.

axis is aligned with the optical axis, $\theta = \pi/2$. The measured points then can be fit to the parametric form [12]

$$d_p^*(\theta) = [\max(d_p^*) - \min(d_p^*)] \sin \theta + \min(d_p^*), \quad (8)$$

$$n_p^*(\theta) = n_m + \frac{\Delta n}{\kappa d_p^*(\theta) - 1}, \quad (9)$$

where $\max(d_p^*) = 3.66 \mu\text{m}$ and $\min(d_p^*) = 1.69 \mu\text{m}$ are the largest and smallest values of $d_p^*(\theta)$ observed in the characterization data, respectively, $n_m = 1.34$ is the refractive index of water, and $\Delta n = 0.023 \pm 0.001$ and $\kappa = (1.18 \pm 0.03) \mu\text{m}^{-1}$ are fitting parameters. The minimum and maximum values of d_p^* may be interpreted as the particle's approximate minor and major axes, which suggests that the particle has an overall aspect ratio of 2.2. The fit is plotted as a dashed curve in Fig. 4(a). Each data point is assigned the polar angle, $\theta(t)$, that minimizes the distance from $(d_p^*(t), n_p^*(t))$ to the fit curve. The data points in Fig. 4(a) are colored accordingly.

Following this procedure, the sequence of measured effective-sphere characterization results can be recast into the angular trajectory that is plotted in Fig. 4(b). This trajectory, in turn, can be used to estimate the particle's rotational diffusion coefficient through the Stokes-Einstein relation [28] taking into account the measurement error, ϵ , in the particle's orientation, $\theta(t)$:

$$\langle \cos \Delta\theta(\tau) \rangle = \exp(-D_\theta \tau) + \epsilon \sqrt{2 \langle \sin^2 \Delta\theta(\tau) \rangle}. \quad (10)$$

Here, $\Delta\theta(\tau) = \theta(t + \tau) - \theta(t)$ and angle brackets indicate averages over t . Values of $\langle \cos \Delta\theta(\tau) \rangle$ computed

from $\theta(t)$ are plotted as discrete points in Fig. 4(c). Fitting these points to Eq. (10) yields the solid curve, $D_\theta = (0.019 \pm 0.001) \text{s}^{-1}$. The corresponding particle diameter, $d_p = (4.1 \pm 0.1) \mu\text{m}$, is consistent with the optically-inferred major axis of the particle, which is expected for rotational diffusion of fractal clusters [29]. The fit also yields an uncertainty of $\epsilon = (5.3 \pm 0.1)^\circ$ in the effective-sphere measurement of this aggregate's orientation angle.

The effective-sphere approach to holographic rotation tracking works best for clusters with the largest aspect ratios, typically those with the smallest fractal dimensions. Reasonable outcomes for particles such as the typical example in Fig. 4 serve to validate the overall structural analysis of this common class of colloidal particles. It also suggests that such particles can be recognized and differentiated from other sorts of particles, such as colloidal spheres, without invoking *a priori* knowledge of their structure and composition.

V. TOWARD HOLOGRAPHIC TOMOGRAPHY

The methods we have described use holograms recorded over a range of orientations to describe the overall structure of fractal colloidal aggregates under the assumption that they actually are fractal. This approach can be extended to obtain more detailed information about the inner structure of such objects. The volume of the bounding effective sphere can be subdivided into voxels characterized by a set of refractive indexes, $\{n_j\}$, that can be used to compute the scattering T matrix for the particle [15]. The T matrix then can be used to compute the particle's hologram as a function of orientation, Ω . In principle, $\{n_j\}$ can be selected to optimize agreement between these synthetic holograms and the set of experimental holograms in random orientations. The optimized model not only would provide direct insights into the distribution of matter within the particle, but also could be used to estimate Ω for the cluster. This optimization scheme currently is too computationally expensive for practical implementation. It may be possible to accelerate convergence by adapting machine-learning techniques for analyzing sequences of single-particle holograms [30].

VI. DISCUSSION

Our results demonstrate that effective-sphere analysis of holographic microscopy data can provide useful information about the morphology of individual fractal clusters. Rather than relying on population averages, this approach draws insights from the distribution of effective-sphere characterization results obtained as the particle rotates in three dimensions. Rather than yielding particular values for the diameter and refractive index, effective-sphere analysis of a rotating fractal aggregate yields estimates for the particle's fractal dimen-

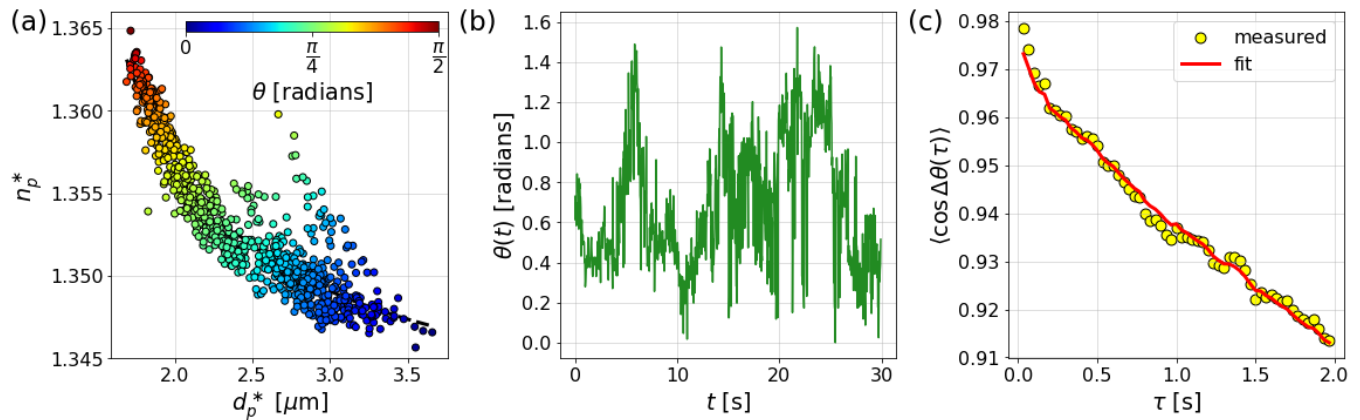


FIG. 4. (a) Effective-sphere characterization data for the particle from Fig. 2(c) colored according to inferred polar angle, θ . (b) Angular trajectory, $\theta(t)$. (c) Mean-square displacement of the orientation unit vector as a function of lag time, τ , together with a fit to Eq. (10) for the particle’s rotational diffusion coefficient, D_θ , and the uncertainty, ϵ , in the measured orientation angle. The dashed curve shows the naive fit that does not account for measurement errors.

sion, its aspect ratio, and its rotational diffusion coefficient. When applied to aggregates of well-characterized monomers this information offers insights into the mechanisms for those clusters’ formation.

The wealth of information provided by holographic particle characterization should be useful in any industry where particle properties affect commercial success. Holographic characterization probes particles in their native media without extensive sample preparation, which is an advantage relative to standard techniques such as electron microscopy. The ability to differentiate fractal aggregates from other types of particles in heterogeneous real-world dispersions sets holographic characterization apart from conventional light-scattering techniques. Holographic characterization is fast enough, moreover, for applications in process control and quality assurance. The population-averaged measurements in Fig. 3(a) and (b) required less than 15 min each, and multi-angle characterization of a colloidal cluster takes just a few seconds thanks to the recent introduction of software for real-time hologram analysis [31].

FUNDING

This work was primarily supported by the SBIR program of the National Institutes of Health under Award Number R44TR001590. The Spheryx xSight, LS Instru-

ments LS Spectrometer, and Malvern Zetasizer Nano ZS were acquired as shared instrumentation by the NYU MRSEC with support from the National Science Foundation under Award Number DMR-1420073. The custom holographic characterization instrument was constructed with support from the MRI program of the NSF under Award Number DMR-0923251.

ACKNOWLEDGMENTS

We are grateful to Prof. Andrew Hollingsworth for assistance with the preparation and light-scattering characterization of the fractal aggregates used in this study.

DISCLOSURES

DGG is a founder of Spheryx, Inc., the company that manufactures the xSight particle-characterization instrument used in this study.

DATA AVAILABILITY

Data underlying the results presented in this paper are not publicly available at this time but may be obtained from the authors upon reasonable request.

[1] A. Winters, F. C. Cheong, M. A. Odete, J. Lumer, D. B. Ruffner, K. I. Mishra, D. G. Grier and L. A. Philips. “Quantitative differentiation of protein aggregates from other subvisible particles in viscous mixtures through holographic characterization.” *J. Pharm. Sci.* **109**, 2405–2412 (2020).

[2] F. C. Cheong, P. Kasimbeg, D. B. Ruffner, E. H. Hlaing, J. M. Blusewicz, L. A. Philips and D. G. Grier. “Holographic characterization of colloidal particles in turbid media.” *Appl. Phys. Lett.* **111**, 153702 (2017).

[3] V. Bianco, D. Pirone, P. Memmolo, F. Merola and P. Ferraro. “Identification of Microplastics Based on the Frac-

- tal Properties of Their Holographic Fingerprint.” *ACS Photonics* (2021).
- [4] H. M. Lindsay, M. Y. Lin, D. A. Weitz, P. Sheng, Z. Chen, R. Klein and P. Meakin. “Properties of fractal colloid aggregates.” *Faraday Discuss. Chem. Soc.* **83**, 153–165 (1987).
- [5] R. Xu. *Particle characterization: light scattering methods*, vol. 13 (Springer Science & Business Media, 2001).
- [6] J. Fung and S. Hoang. “Computational assessment of an effective-sphere model for characterizing colloidal fractal aggregates with holographic microscopy.” *J. Quant. Spectrosc. Radiat. Transf.* **236**, 106591 (2019).
- [7] C. Wang, F. C. Cheong, D. B. Ruffner, X. Zhong, M. D. Ward and D. G. Grier. “Holographic characterization of colloidal fractal aggregates.” *Soft Matter* **12**, 8774–8780 (2016).
- [8] C. Wang, X. Zhong, D. B. Ruffner, A. Stutt, L. A. Philips, M. D. Ward and D. G. Grier. “Holographic characterization of protein aggregates.” *J. Pharm. Sci.* **105**, 1074–1085 (2016).
- [9] M. A. Odete, F. C. Cheong, A. Winters, J. J. Elliott, L. A. Philips and D. G. Grier. “The role of the medium in the effective-sphere interpretation of holographic particle characterization data.” *Soft Matter* **16**, 891–898 (2020).
- [10] R. W. Perry, G. Meng, T. G. Dimiduk, J. Fung and V. N. Manoharan. “Real-space studies of the structure and dynamics of self-assembled colloidal clusters.” *Faraday Discuss.* **159**, 211–234 (2012).
- [11] S.-H. Lee, Y. Roichman, G.-R. Yi, S.-H. Kim, S.-M. Yang, A. Van Blaaderen, P. Van Oostrum and D. G. Grier. “Characterizing and tracking single colloidal particles with video holographic microscopy.” *Opt. Express* **15**, 18275–18282 (2007).
- [12] L. E. Altman, R. Quddus, F. C. Cheong and D. G. Grier. “Holographic characterization and tracking of colloidal dimers in the effective-sphere approximation.” *Soft Matter* **17**, 2695–2703 (2021).
- [13] J. Sheng, E. Malkiel and J. Katz. “Digital holographic microscope for measuring three-dimensional particle distributions and motions.” *Appl. Opt.* **45**, 3893–3901 (2006).
- [14] C. F. Bohren and D. R. Huffman. *Absorption and Scattering of Light by Small Particles* (John Wiley & Sons, 2008).
- [15] M. I. Mishchenko, L. D. Travis and A. A. Lacis. *Scattering, Absorption, and Emission of Light by Small Particles* (Cambridge University Press, 2002).
- [16] G. Gouesbet and G. Gréhan. *Generalized Lorenz-Mie Theories*, vol. 31 (Springer, 2011).
- [17] B. J. Krishnatreya, A. Colen-Landy, P. Hasebe, B. A. Bell, J. R. Jones, A. Sunda-Meya and D. G. Grier. “Measuring Boltzmann’s constant through holographic video microscopy of a single colloidal sphere.” *Am. J. Phys.* **82**, 23–31 (2014).
- [18] A. Wang, T. G. Dimiduk, J. Fung, S. Razavi, I. Kretzschmar, K. Chaudhary and V. N. Manoharan. “Using the discrete dipole approximation and holographic microscopy to measure rotational dynamics of non-spherical colloidal particles.” *J. Quant. Spectrosc. Radiat. Transf.* **146**, 499–509 (2014).
- [19] S. Barkley, T. G. Dimiduk, J. Fung, D. M. Kaz, V. N. Manoharan, R. McGorty, R. W. Perry and A. Wang. “Holographic microscopy with Python and HoloPy.” *Comput. Sci. Eng.* **22**, 72–82 (2019).
- [20] V. A. Markel. “Introduction to the Maxwell Garnett approximation: tutorial.” *JOSA A* **33**, 1244–1256 (2016).
- [21] F. C. Cheong, K. Xiao, D. J. Pine and D. G. Grier. “Holographic characterization of individual colloidal spheres’ porosities.” *Soft Matter* **7**, 6816–6819 (2011).
- [22] M. Hannel, C. Middleton and D. G. Grier. “Holographic characterization of imperfect colloidal spheres.” *Appl. Phys. Lett.* **107**, 141905 (2015).
- [23] M. J. O’Brien and D. G. Grier. “Above and beyond: holographic tracking of axial displacements in holographic optical tweezers.” *Opt. Express* **27**, 25375–25383 (2019).
- [24] F. C. Cheong, B. S. R. Dreyfus, J. Amato-Grill, K. Xiao, L. Dixon and D. G. Grier. “Flow visualization and flow cytometry with holographic video microscopy.” *Opt. Express* **17**, 13071–13079 (2009).
- [25] L. Dixon, F. C. Cheong and D. G. Grier. “Holographic particle-streak velocimetry.” *Opt. Express* **19**, 4393–4398 (2011).
- [26] T. A. Witten and L. M. Sander. “Diffusion-limited aggregation.” *Phys. Rev. B* **27**, 5686 (1983).
- [27] P. Meakin, I. Majid, S. Havlin and H. E. Stanley. “Topological properties of diffusion limited aggregation and cluster-cluster aggregation.” *J. Phys. A* **17**, L975 (1984).
- [28] R. Jain and K. Sebastian. “Diffusing diffusivity: Rotational diffusion in two and three dimensions.” *J. Chem. Phys.* **146**, 214102 (2017).
- [29] M. Lattuada, H. Wu and M. Morbidelli. “Rotational diffusivity of fractal clusters.” *Langmuir* **20**, 5630–5636 (2004).
- [30] B. Midtvedt, E. Olsén, F. Eklund, F. Höök, C. B. Adiels, G. Volpe and D. Midtvedt. “Fast and accurate nanoparticle characterization using deep-learning-enhanced off-axis holography.” *ACS Nano* **15**, 2240–2250 (2021).
- [31] L. E. Altman and D. G. Grier. “CATCH: Characterizing and tracking colloids holographically using deep neural networks.” *The Journal of Physical Chemistry B* **124**, 1602–1610 (2020).